Study of the oxygen reduction reaction on pure and Zr-doped $YMnO_{3+\delta}$ SOFC electrode

Zulma L. Moreno Botello , Alejandra Montenegro-Hernández , Liliana Mogni , Gilles H. Gauthier

PII: S0013-4686(20)31725-4
DOI: https://doi.org/10.1016/j.electacta.2020.137332
Reference: EA 137332

To appear in: *Electrochimica Acta*

Received date: 20 April 2020
Revised date: 6 October 2020
Accepted date: 19 October 2020

Please cite this article as: Zulma L. Moreno Botello , Alejandra Montenegro-Hernández , Liliana Mogni , Gilles H. Gauthier , Study of the oxygen reduction reaction on pure and Zr-doped $YMnO_{3+\delta}$ SOFC electrode, *Electrochimica Acta* (2020), doi: https://doi.org/10.1016/j.electacta.2020.137332

Highlights

- The layered (Y,Zr)MnO_3 manganites are studied as SOFC cathode.
- A Gerischer-type element stems from to an oxygen ion diffusion and a surface limiting process.
- A LF R//CPE element is attributed to dissociation of the chemisorbed O_2 on $YMnO_3$.
- The same LF process is related to O_2 gas diffusion/physisorption for $Y_{0.9}Zr_{0.1}MnO_3$.
- The ORR mechanism is influenced by Zr-doping in both electrical and surface properties.

Study of the oxygen reduction reaction on pure and Zr-doped $YMnO_{3+\delta}$ SOFC electrode

Zulma L. Moreno Botello[a,b], Alejandra Montenegro-Hernández[b], Liliana Mogni[b,*], Gilles H. Gauthier[a,*]

[a] Universidad Industrial de Santander, Grupo INTERFASE, Ciudad universitaria, Calle 9, Carrera 27, Bucaramanga (Santander), Colombia.

[b] INN-CNEA-CONICET, Centro Atómico Bariloche, Av. Bustillo 9500, S. C. de Bariloche, Rio Negro, 8400, Argentina.

* Corresponding author: Email: mogni@cab.cnea.gov.ar (Liliana Mogni); Phone: (+57) 734 4000 ext. 2528, Email: gilgau@uis.edu.co (Gilles Gauthier).

Credit Author Statement

- **Zulma L. Moreno Botello:** Investigation, Formal analysis, Visualization, Writing - Original Draft.
- **Alejandra Montenegro-Hernández:** Investigation, Resources, Formal analysis, Supervision, Writing, Reviewing and Editing.
- **Liliana Mogni:** Methodology, Supervision, Conceptualization, Writing, Reviewing and Editing.
- **Gilles H. Gauthier:** Methodology, Supervision, Conceptualization, Writing, Reviewing and Editing.

Abstract

The effect of Zr-doping on the novel SOFC cathode $YMnO_3$ and its O_2-Reduction Reaction (ORR) was studied using electrochemical impedance spectroscopy (EIS) as a function of temperature (500 < T <800 ºC) and the oxygen partial pressure (10^{-4} < pO_2 < 1 atm). EIS technique allows identifying three processes controlling the ORR for each electrode, differentiated by their characteristic frequency, activation energies and pO_2 dependence. High frequency contribution, only observed at 600 °C for both electrodes, was attributed to oxygen ion transfer trough the electrode/electrolyte interface. In both electrodes, the Intermediate frequency contribution was described by a Gerischer impedance, related to a co-limiting process between oxygen ion diffusion and a surface process. However, whereas the EIS characteristics for $YMnO_3$ can be explained by a surface process controlled by the electron transfer from oxide to O-adsorbed, it seems related for $Y_{0.9}Zr_{0.1}MnO_3$ to the probability of finding a second free-surface site near to a diatomic intermediated for the O_2 dissociation. These differences are in agreement with the improvement of the electrical properties when $YMnO_3$ is doped with Zr. The low frequency contribution became important as pO_2 decreased and temperature increased, and its characteristics would indicate a secondary surface process, co-limited with O_2 gas diffusion for $Y_{0.9}Zr_{0.1}MnO_3$ porous electrode.

Keywords: Solid Oxide Fuel Cells, Cathode, Zr-doped Yttrium manganite, Electrochemical Impedance Spectroscopy.

1. Introduction

With high efficiency and (fossil or synthetic) fuel flexibility, Solid Oxide Fuel Cells (SOFC) are considered as one of the most promising technologies for energy conversion [1]. The state-of-the-art materials that are used as electrolyte, anode and cathode in SOFC

are Yttria-Stabilized Zirconia (YSZ), Nickel/YSZ composite, referred to as Ni/YSZ cermet, and Sr-doped lanthanum manganite (LSM), respectively; nevertheless, those materials, developed more than thirty years ago, have been designed for an operation temperature that ranges generally between 800 and 1000 °C [1–4]. A lower operating temperature, in the so-called intermediate temperature range (500-700 °C), would bring many advantages such as a decrease of the cost of the system (including the cell and interconnects´ materials) and a dramatic reduction of thermally activated degradation issues that stem basically from cationic interdiffusion between electrode, electrolyte and interconnects during cell preparation and/or *in operando*. But a reduction of the temperature is not possible without the development of new electrode and electrolyte compositions, for which it seems that the cathode limitations are the most critical due to low kinetics of the oxygen reduction reaction (ORR) in absence of an efficient electrocatalyst [4–6].

During the last two decades, many investigations have been focused on the search for new cathode compositions and structures with higher electrochemical activity, but also chemical stability and durability. It is now clear that the state-of-the-art LSM could not be efficient at low temperature, because this material is basically a pure electronic conductor. Even if better performance can be achieved by forming a composite with YSZ electrolyte (similar to the case of Ni/YSZ cermet), it is also clear that the best ORR electrocatalyst should intrinsically exhibit Mixed Ionic and Electronic Conductivity (MIEC) [1–8]. Since the success of LSM, most of the studies concerning new SOFC cathode materials remained based on AMOx oxides with A=La/AE (AE=Alkaline Earth) and M a third-row transition metal (in particular Mn, Fe, Co, Ni and Cu) and a perovskite (or derived) structure. However, these cathodes degrade with time, either by AE segregation on the cathode surface [9,10], or due to interfacial chemical reactions between the electrode and the electrolyte. The first one is induced by the size mismatch between dopant and host

cations, *e.g.* Ba surface segregation is more significant than Sr and Ca surface enrichment for (La,M)MnO_3 with M = Ba, Sr or Ca electrodes [11,12], whereas the second one is due to cations interdiffusion taking place during the cell elaboration or *in operando*, with the formation of electrically insulating phases such as $La_2Zr_2O_7$ and $AEZrO_3$ [7,8,13–18]. Even the use of a ceria-based buffer layer is sometimes not sufficient to avoid such thermodynamically favourable reaction, which is only kinetically limited by lowering the temperature of operation or of electrode sintering, as we could recently evidence in the case of $(La,Sr)_2MnO_4$ Ruddlesden-Popper phases [19]. Other Rare Earth (RE) elements like Pr or Nd, have been proposed to replace La in the composition of AE-free electrode compounds, *e.g.* in the Ruddlesden Popper nickelates $RE_2NiO_{4+\delta}$ (RE= Pr,Nd), expecting less reactivity with YSZ electrolytes due to the decreasing stability of the pyrochlore phase $RE_2Zr_2O_7$ along the lanthanide series [20–23]. The chemical reactivity was effectively decreased but did not totally disappear, making long term stability or high temperature thermal treatments at T>1000 °C, generally requested for the cell preparation, a subject of particular concern for the use of such kind of materials [24,25].

Considering the chemical and structural richness of the transition metal oxides, in particular the manganites [26–28], recently we reported a study of fully YSZ-compatible electrode materials avoiding basically La/AE elements in their composition [29,30]. In particular, yttrium manganites with $YMnO_{3+\delta}$ composition have caught our attention for several reasons: (i) Y is a constitutive element of state-of-the-art YSZ electrolyte and does not form any pyrochlore zirconate phase in SOFC cell elaboration or operating conditions [31], suggesting limited interface degradation and (ii) the material can exhibit large oxygen hyperstoichiometry and a reversible capacity to store different quantities of oxygen [32–34]. Excepting particular synthesis conditions (far from SOFC application), the structure of small Rare Earth (RE) manganites (RE=Dy-Lu, Y, Sc) is not a perovskite. The layered

structure with space group $P6_3cm$ is built of layers of Y^{3+} ions and MnO_5 trigonal bipyramids, in which the corner-sharing polyhedra form a triangular network in the basal plane *ab* (Fig. 1) [35–38].

In our previous work, we explored the possibility to substitute Zr for Y in $YMnO_{3+\delta}$ and confirm a solubility limit around x=0.1 using solid-state synthesis route [30] as well as the perfect chemical compatibility between $Y_{1-x}Zr_xMnO_{3+\delta}$ (YZM) and YSZ electrolyte. In a more recent study [29], we performed an in-depth structural characterization of $Y_{1-x}Zr_xMnO_{3+\delta}$ compounds, prepared by a sol-gel Pechini-type route, and addressed in particular the charge equilibrium in the Zr-doped compounds. Zirconium was found to both stabilize the excess oxygen compared to pure $YMnO_3$ and possibly provide an oxygen ion migration path with a lower energy barrier, the symmetry of the crystal structure being increased to the $P6_3/mmc$ space group; the main consequence of Zr-doping on the structure is the absence of [Mn-O] corrugated layers evidenced in Fig. 1 for undoped $YMnO_3$. A possible MIEC behaviour in Zr-doped $YMnO_{3+\delta}$ was suggested by both the conductivity measurements and theoretical calculations. The initial EIS measurements were very promising, confirming the YZM potential as cathode material for Solid Oxide Fuel Cells.

The present article deals with a study of the electrochemical characteristics of $YMnO_3$ and the effect on these of the partial substitution of Y by Zr, $Y_{0.9}Zr_{0.1}MnO_{3+\delta}$. The potential use of these materials as SOFC cathode is analyzed by studying the mechanism of the O_2-reduction reaction at 600, 700 and 800 °C, and its correlation with high temperature transport properties previously reported [25].

2. Experimental.

Powders of $YMnO_3$ and $Y_{0.9}Zr_{0.1}MnO_3$ were synthetized by using the Pechini route from metal precursors in the form of nitrates, carbonates and oxides, as discussed elsewhere [29]. The powders were pressed into pellets which were heat treated in air, at 1100 °C ($YMnO_3$) or 1200°C (Zr-doped sample) for 12 hours, with a heating ramp of 5°C min^{-1}. Phase purity was confirmed by X-ray powder diffraction (BRUKER D8 ADVANCE powder diffractometer working in Bragg Brentano geometry with Cu-Kα radiation and 1D LynxEye detector).

The electrochemical performance of porous $YMnO_3$ and $Y_{0.9}Zr_{0.1}MnO_3$ (YZM) electrodes was achieved by Electrochemical Impedance Spectroscopy (EIS). This characterization was carried out on dense Yttria-Stabilized Zirconia (YSZ) electrolytes, using a symmetrical LSM/YZM/YSZ/YZM/LSM cell configuration. LSM stands for $La_{0.2}Sr_{0.8}MnO_3$ perovskite material, used here as current collector. Symmetrical cells were prepared by depositing a porous layer of YZM on both sides of a dense YSZ pellets. Dense YSZ electrolyte (~ 1 cm diameter) were obtained pressing commercial YSZ (TZ-8Y, Tosoh Corporation) sintered at 1300°C for 6 h. YZM powders were dispersed with polyvinyl butyral (1.7 % w/w), Polyvinylpyrrolidone (0.9 % w/w), isopropanol (38.8 % w/w) and α- terphineol (23.6 % w/w). The YSZ substrates were covered onto both flat sides with the as-obtained YZM ink using spin coating technique. Afterwards, the symmetrical assemblies were heat treated at 1150 °C for 3 h in air to promote electrode/electrolyte adhesion. The microstructure homogeneity and electrode thickness were studied with Scanning Electronic Microscopy (SEM) using an FEI Nova NanoSEM 230 microscope.

EIS measurements were performed using a frequency response analyzer (FRA) coupled to an AUTOLAB potentiostat. EIS spectra were recorded in the temperature range from 500 up to 800 ºC in dry air. Also, at 600, 700 and 800 °C, EIS spectra were collected

varying the oxygen partial pressure (pO_2) within the range of 10^{-4} to 1 atm, using Ar as gas carrier. Controlled pO_2 atmospheres were provided by an electrochemical system composed of an oxygen pump and an oxygen sensor [39]. The resulting spectra were fitted with electrical equivalent circuit using a MatLab code [40].

3. Results and discussion.

Figure 2(a) and 2(b) show SEM micrographs of the porous YZM electrodes deposited on the dense YSZ electrode and covered with the LSM current collector. Figures 2(c) and 2(d) show a detail of the pure and Zr-doped YSM/YSZ interfaces, respectively. The electrodes present agglomerated particles with large size (~0.5-1 μm). A good electrode-electrolyte contact is achieved, no cracks were observed for the studied cathodes and the cross sections show a film thickness of approximately 25-30 μm for both electrodes.

Recently, we reported a preliminary electrochemical study of YZM as a function of temperature [29]. In that work, we found that, despite the higher electrical conductivity of the Zr-doped sample (*e.g.* σ at 800 ºC are 0.01 and 0.2 S cm^{-1} for $YMnO_3$ and $Y_{0.9}Zr_{0.1}MnO_3$, respectively), the area specific resistance (ASR) obtained from EIS measurements for $YMnO_3$-based cell were lower than those of $Y_{0.9}Zr_{0.1}MnO_3$-based cell (*e.g.* ASR at 800°C in air are 0.21 and 0.83 Ω cm^2 for $YMnO_3$ and $Y_{0.9}Zr_{0.1}MnO_3$, respectively). In that previous work, we found that optimum adhesion temperature between $Y_{0.9}Zr_{0.1}MnO_3$ electrode and YSZ electrolyte is 1100ºC. However, in order to perform a better comparison, we decided to focus the present study on the oxygen reduction reaction measured for electrodes treated at the same adhesion temperature of 1150 °C.

Figure 3 shows the dependence of ASR for LSM/$YMnO_3$/YSZ/$YMnO_3$/LSM and LSM/$Y_{0.9}Zr_{0.1}MnO_3$/YSZ/$Y_{0.9}Zr_{0.1}MnO_3$/LSM cells with temperature in air. The ASR values

for $YMnO_3$ cells are lower than those of $Y_{0.9}Zr_{0.1}MnO_3$ in the whole range of temperature. Previously, we found that the EIS spectra collected in air present two well distinguished arcs (not shown here) [29]. The contribution observed at frequencies higher than 10^1 Hz disappears from 600°C; then, this arc was associated to the electrolyte impedance [41]. Consequently, only the low frequency contribution can be associated with the Oxygen Reduction Reaction (ORR) taking place at the electrode. In order to determine the processes involved in the ORR for the cathode materials, the symmetrical cells were measured at different oxygen partial pressures ($10^{-4} \leq pO_2 \leq 1$ atm) for T= 600, 700 and 800 °C.

Figures 4, 5 and 6 show the evolution of the EIS spectra collected for $YMnO_3$ and $Y_{0.9}Zr_{0.1}MnO_3$ electrodes as a function of pO_2 at 600, 700 and 800 °C, respectively. The EIS spectra increase as pO_2 decreases, which is expected due to limitation of oxygen reactive species. The shape of the spectra for Zr-doped manganite are different from the cell with $YMnO_3$; this fact is related to the different limiting steps controlling the oxygen reduction at each electrode. At high pO_2, $YMnO_3$ presents a lower impedance than $Y_{0.9}Zr_{0.1}MnO_3$. However, at 600 and 700 °C, the impedance of $YMnO_3$ increases more than for $Y_{0.9}Zr_{0.1}MnO_3$ as pO_2 decreases. Therefore, the impedance of $YMnO_3$ exceeds that of $Y_{0.9}Zr_{0.1}MnO_3$ at low pO_2 values. Also, at all temperatures, the maximum relaxation frequencies for $YMnO_3$ are higher than for $Y_{0.9}Zr_{0.1}MnO_3$.

Nyquist and Bode plots at 600 and 700 ºC in the case of $YMnO_3$ cell (Figures 4(a), a(b), 5(a) and 5(b)) show only one maximum of relaxation frequency, suggesting that the mechanism limiting the oxygen reduction reaction is controlled by a single step in the whole pO_2 range. However, at 800 °C, the existence of two processes is evident, especially at low pO_2, where a second arc is easily distinguishable (Figures 6(a) and 6(b)). On the contrary, Nyquist and Bode plots for $Y_{0.9}Zr_{0.1}MnO_3$ cell indicate the presence of two

processes at 600, 700 and 800 °C (Figures 4(c), 4(d) 5(c), 5(d), 6(c) and 6(d)). However, in order to clarify how many mechanisms are controlling the ORR, the spectra obtained were fitted using equivalent electrical circuits (EEC). The best fit results for both electrodes were obtained with the EEC composed by: an inductive element (L_1) due to the inductance of the wires, an ohmic resistance (R_1) that corresponds to the electrolyte resistance, a high frequency parallel combination of one resistance and one constant phase element (R//CPE), only present at 600 °C, a Gerischer-type element (G), that describes the contribution at intermediate frequencies, and a R//CPE element at low frequencies. However, in the cases where the polarization resistance that corresponds to the R//CPE element (R_{Cpe}) is negligible, the spectra were fitted by a unique G element (*e.g.* for $2x10^{-2}<pO_2<1$ atm).

Figure 7 shows the evolution of the polarization resistance with the oxygen partial pressure pO_2 for each component of the EEC in the case of both $YMnO_3$ and $Y_{0.9}Zr_{0.1}MnO_3$ electrodes and at T=600, 700 and 800°C. The polarization resistance of the high frequency contribution, only observed at 600°C for both electrodes, was not included in Figure 7. This impedance is negligible in comparison with the intermediate and low frequencies and exhibits capacitances values of $C\sim10^{-5}$ F/cm^2, which can be associated with a process of ionic transfer. Therefore, as explained above, this contribution can be attributed with greater certainty to the ionic intergranular resistance of the electrolyte, due to the fact that YSZ electrolyte exhibits low ionic conductivity values at T≤ 600°C. Given that the YSZ conductivity increases with temperature, such contribution disappears at higher temperatures and is not usually taken into account for electrode reaction analysis [42,43].

Figures 8(a) shows the Arrhenius plot of the Gerischer polarization resistance component (R_G) at low ($6\ 10^{-4}$ atm) and high (0.2 atm) pO_2. Figure 8(b) shows the

Arrhenius plot, for the low frequency component (R_{Cpe}), only observed at low pO_2. Table 1 summarizes the main characteristics of the impedance response. At high pO_2, similar values of activation energies (E_a) were obtained for R_G, *i.e.* 1.03 and 0.99 eV, for $YMnO_3$ and $Y_{0.9}Zr_{0.1}MnO_3$, respectively. At low pO_2, the E_a obtained for R_G differs from 1.27 eV for $YMnO_3$ to 0.56 eV for $Y_{0.9}Zr_{0.1}MnO_3$ electrode. On the contrary, for the low frequencies R_{Cpe} contribution, the E_a of the $Y_{0.9}Zr_{0.1}MnO_3$ sample (0.57 eV) is higher than of undoped one (0 eV).

The intermediate frequency Gerischer impedance (Z_G) shows the largest difference between both electrodes. Figure 7 shows that, except at high pO_2, the R_G values of the Zr-doped $YMnO_3$ is higher than those of the undoped electrode. Also, the Gerischer element pO_2 dependence is R_G α $pO_2^{-0.5}$ for $YMnO_3$, and R_G α $pO_2^{-0.25}$ for $Y_{0.9}Zr_{0.1}MnO_3$. The different pO_2 dependence indicates a change of limiting step in the O_2 reduction reaction when $YMnO_3$ is doped with Zr. This is also supported by the different activation energies, which is twice higher for $YMnO_3$ than for $Y_{0.9}Zr_{0.1}MnO_3$ at low pO_2. The Gerischer-type impedance arises from solving the diffusion equation for a semi-finite medium, in which the concentration on the surface is controlled by a surface oxygen exchange reaction [44]. Thus, the Gerischer-type impedance can be described more accurately as a co-limiting process between the oxygen exchange at the electrode/gas surface and the oxygen ion diffusion, either in the surface or the bulk of materials [45–47]. This model was adapted for a porous single-phase MIEC and depends on the concentration and diffusivity of vacancies within the electrode's bulk [48]. Then, Gerischer impedance has been found in mixed conducting electrodes even with poor electronic conductivity, as those made of lanthanum chromite/titanate. Therefore, it is not surprising to find this electrochemical behavior in electrodes with $YMnO_3$, which exhibits a low electronic conductivity, but might have a high ionic conductivity. The co-limiting origin of the Gerischer impedance gives

place to a convoluted resistance $R_G = \sqrt{R_D R_S}$, where R_D refers to the O-diffusion resistance and R_S the resistance associated to the surface process. From table 1, it can be noted that both samples exhibit capacitances values around C~10^{-2}-10^{-1} F cm^{-2}, which are consistent with the fact that surface plays an important role in the oxygen reduction mechanism of both samples. However, whereas the dependence of R_G with pO_2 for $YMnO_3$ (n =-1/2) is consistent with a surface process controlled by the chemisorption of O_2, the dependence observed of $Y_{0.9}Zr_{0.1}MnO_3$ (n= –1/4) suggests that the controlling surface process is dominated by the O_2-disociative adsorption. In the first case (n =-1/2 for $YMnO_3$), the surface process is mediated by a highly unstable physisorbed diatomic intermediated, which is transformed to a more stable diatomic superoxide intermediate ($O_2 + V_{O,s}^{\cdot\cdot} + e - \rightleftharpoons (O_2)_{O,s}^{\cdot}$; $R_S \propto pO_2$). This process is limited by the energy barrier for the electron transfer process, *i.e.* is characterized by a high activation energy beyond 1 eV for $YMnO_3$ [49]. When $YMnO_3$ is doped, the partial substitution of Y^{+3} for Zr^{+4} increases the electronic transport and the O-interstitials defect concentration [29], leading to a change of mechanism to a surface reaction mediated by a highly unstable physisorbed diatomic intermediate, which is transformed to a more stable single-atomic adsorbed intermediate ($O_2 + s \rightarrow O_{2,s} + s + 4e \xrightarrow{limiting} 2O_s^{-2}$, $R_S \propto pO_2^{0.5}$). The surface process is then limited by the probability of finding an available second surface site (*s*) near to the diatomic intermediate [49]. The dissociative-adsorption has lower activation energy than those involving charge transfer, due only to the enthalpy of dissociation.

Finally, as well the Gerischer element, the low frequency contribution described by the R//CPE element exhibits some differences between the pure and the doped sample. In general, the pO_2 dependence (R_{Cpe} α $pO_2^{-0.5}$-$pO_2^{-0.75}$) and the capacitances values (C~0.05-0.01 F cm^{-2}) for $YMnO_3$ are lower than the respective values for the Zr-doped sample (R_{Cpe} α $pO_2^{-0.75}$-pO_2^{-1} and C~0.1-1 F cm^{-2}). These differences suggest a

competition between O_2-gas diffusion (large capacitance value and R α pO_2^{-1}) and a surface process. Then, for $Y_{0.9}Zr_{0.1}MnO_3$ the low frequency impedance behavior is in agreement with a limiting step due to O_2-gas diffusion, whereas for $YMnO_3$, the n value, the capacitances and the fact that such impedance appears at low frequency allows associating it with an oxygen dissociative adsorption process on the electrode surface [50,51]. Summarizing, the impedance results suggest that the O_2-reduction mechanism is controlled by $O_2 + s + e \xrightarrow{co-limiting\ Z_G} O_{2,s}^- + s + 3e \xrightarrow{limiting\ Z_{R//Cpe}} 2O_s^{-2}$ for $YMnO_3$ sample and $O_{2,gas} \xrightarrow{limiting\ Z_{R//Cpe}} O_{2,pore} + s \rightarrow O_{2,s} + s + 4e \xrightarrow{co-limiting\ Z_G} 2O_s^{-2}$ for $Y_{0.9}Zr_{0.1}MnO_3$. Then, whereas the reaction for $YMnO_3$ is limited by two charge transfer steps, the Zr substitution facilitates these processes. However, Zr also increases the number of O-interstitials, which can block the free surface sites required for the O_2 dissociation.

4. **Conclusions**

The study of the electrochemical performance of $YMnO_3$ and $Y_{0.9}Zr_{0.1}MnO_3$ by EIS, using YSZ and LSM as electrolyte and current collector, respectively, allow to obtain original information about the mechanisms involved in the oxygen reduction reaction of these novel SOFC porous electrodes. The EIS spectra, recorded in the temperature range from 500 up to 800 °C in dry air, and at 600, 700 and 800 °C, varying the pO_2 within the range of 10^{-4} to 1 atm, were fitted using an EEC. The best fit results for both electrodes were obtained with the EEC composed by an inductive element, an ohmic resistance, a Gerischer-type element being the main contribution at intermediate frequency and two parallel combinations of one resistance and one constant phase element (R//CPE), one at high frequency only present at 600 °C and the other one at low frequency mainly observed

at low pO_2 and high temperature. The ohmic resistance and the high frequency R//CPE correspond to the electrolyte resistance and the oxygen ion transfer trough the electrode/electrolyte interface, respectively. The Gerischer-type element is related to a co-limiting process between oxygen ion diffusion and a surface process. For the $YMnO_3$ electrode, the surface process was attributed to electron transfer to a diatomic adsorbed specie (O_2-chemisorption), while for $Y_{0.9}Zr_{0.1}MnO_3$, was attributed to the probability of finding a second free-surface site near to the diatomic intermediated to assist the molecular dissociation (dissociative adsorption). The low frequencies R//CPE element is attributed to dissociation of the chemisorbed O_2 on $YMnO_3$ electrode and to O_2 gas diffusion/physisorption for $Y_{0.9}Zr_{0.1}MnO_3$ sample. The differences observed in the ORR mechanism were associated to the increase of both the electronic transport and increasing of the O-interstitials concentration due to the partial substitution of Zr^{4+} for Y^{3+} in the doped $YMnO_3$ sample.

Declaration of Competing Interest

The authors declare that they have no known competing financial interests or personal relationships that could have appeared to influence the work reported in this paper.

Acknowledgments

The authors acknowledge the financial support of the Colombian Administrative Department of Science, Technology and Innovation COLCIENCIAS (Project # 110265842833 "*Symmetrical high temperature Fuel Cell operating with Colombian natural gas*" (contract # 038-2015) and Project "S*tudy of nanostructured mixed oxides with layered crystal structure as electrode materials for Solid Oxide fuel Cells*" (contract # RC 611-2014)), of the Ministry of Science, Technology and Productive Innovation (MINCYT) and the National Scientific and Technical Research Council (CONICET) of Argentina (Bilateral Cooperation Program with COLCIENCIAS, Project "S*tudy of nanostructured mixed oxides with layered crystal structure as electrode materials for Solid Oxide fuel Cells*"), UIS'

Vicerrectorship for Investigation and Extension (Projects # 9448 and # 9449), the technical support of UIS' X-Ray Laboratory (Parque Tecnológico Guatiguará) for XRD measurements. Zulma Moreno Botello acknowledges UIS and in particular the School of Metallurgy and Materials Science for the Ph.D. scholarship. The authors express their personal thanks to Alberto Caneiro for useful discussions and to Jesús Vega and Diana Garcés from CNEA/CAB for their technical advices.

References.

[1] S.C. Singhal, Solid oxide fuels cells : facts and figures : past, present and future perspectives for SOFC technologies, Springer, London, 2013. https://doi.org/10.1007/978-1-447-14456_1.

[2] Z. Shao, M.O. Tadé, Cathodes for IT-SOFCs, in: 2016: pp. 59–126. https://doi.org/10.1007/978-3-662-52936-2_3.

[3] N. Minh, J. Mizusaki, S.C. Singhal, Advances in Solid Oxide Fuel Cells: Review of Progress through Three Decades of the International Symposia on Solid Oxide Fuel Cells, ECS Trans. 78 (2017) 63–73. https://doi.org/10.1149/07801.0063ecst.

[4] W.H. Kan, A.J. Samson, V. Thangadurai, Trends in electrode development for next generation solid oxide fuel cells, J. Mater. Chem. A. 4 (2016) 17913–17932. https://doi.org/10.1039/C6TA06757C.

[5] Z. Gao, L. V. Mogni, E.C. Miller, J.G. Railsback, S.A. Barnett, A perspective on low-temperature solid oxide fuel cells, Energy Environ. Sci. 9 (2016) 1602–1644. https://doi.org/10.1039/C5EE03858H.

[6] P. Kaur, K. Singh, Review of perovskite-structure related cathode materials for solid oxide fuel cells, Ceram. Int. (2019). https://doi.org/10.1016/j.ceramint.2019.11.066.

[7] H. Tu, U. Stimming, Advances, aging mechanisms and lifetime in solid-oxide fuel cells, J. Power Sources. 127 (2004) 284–293. https://doi.org/10.1016/j.jpowsour.2003.09.025.

[8] T. Ishihara, Structure and Properties of Perovskite Oxides, in: 2009: pp. 1–16. https://doi.org/10.1007/978-0-387-77708-5_1.

[9] D. Garcés, H. Wang, S.A. Barnett, A.G. Leyva, F.R. Napolitano, R.O. Fuentes, H.E. Troiani, L. V. Mogni, An insight into the electrochemical performance of La 0.5−x Pr x Ba 0.5 CoO 3−δ as cathodes for solid oxide fuel cells: study of the O 2 -reduction reaction, J. Mater. Chem. A. 6 (2018) 16699–16709. https://doi.org/10.1039/C8TA04338H.

[10] S.P. Simner, M.D. Anderson, M.H. Engelhard, J.W. Stevenson, Degradation Mechanisms of La–Sr–Co–Fe–O[sub 3] SOFC Cathodes, Electrochem. Solid-State Lett. 9 (2006) A478. https://doi.org/10.1149/1.2266160.

[11] W. Lee, J.W. Han, Y. Chen, Z. Cai, B. Yildiz, Cation Size Mismatch and Charge Interactions Drive Dopant Segregation at the Surfaces of Manganite Perovskites, J. Am. Chem. Soc. 135 (2013) 7909–7925. https://doi.org/10.1021/ja3125349.

[12] W. Lee, J.W. Han, Y. Chen, Z. Cai, B. Yildiz, Cation Size Mismatch and Charge Interactions Drive Dopant Segregation at the Surfaces of Manganite Perovskites, (2011) 2139.

[13] M.M. Kuklja, E.A. Kotomin, R. Merkle, Y.A. Mastrikov, J. Maier, Combined theoretical and experimental analysis of processes determining cathode

performance in solid oxide fuel cells, Phys. Chem. Chem. Phys. 15 (2013) 5443. https://doi.org/10.1039/c3cp44363a.

[14] Y. Chen, W. Zhou, D. Ding, M. Liu, F. Ciucci, M. Tade, Z. Shao, Advances in Cathode Materials for Solid Oxide Fuel Cells: Complex Oxides without Alkaline Earth Metal Elements, Adv. Energy Mater. 5 (2015) 1500537. https://doi.org/10.1002/aenm.201500537.

[15] V. Miguel-Perez, J.P. Ouweltjes, A. Tarancon, M. Torrell, V. Bongiorno, Z. Wuillemin, D. Montinaro, A. Morata, Degradation Studies and Sr Diffusion Behaviour in Anode Supported Cell after 3,000 h SOFC Short Stack Testing, ECS Trans. 68 (2015) 1803–1813. https://doi.org/10.1149/06801.1803ecst.

[16] Z. Yang, M. Guo, N. Wang, C. Ma, J. Wang, M. Han, A short review of cathode poisoning and corrosion in solid oxide fuel cell, Int. J. Hydrogen Energy. 42 (2017) 24948–24959. https://doi.org/10.1016/j.ijhydene.2017.08.057.

[17] J.H. Zhu, H. Ghezel-Ayagh, Cathode-side electrical contact and contact materials for solid oxide fuel cell stacking: A review, Int. J. Hydrogen Energy. 42 (2017) 24278–24300. https://doi.org/10.1016/j.ijhydene.2017.08.005.

[18] F.S. da Silva, T.M. de Souza, Novel materials for solid oxide fuel cell technologies: A literature review, Int. J. Hydrogen Energy. 42 (2017) 26020–26036. https://doi.org/10.1016/j.ijhydene.2017.08.105.

[19] M. V. Sandoval, C. Cárdenas, E. Capoen, C. Pirovano, P. Roussel, G.H. Gauthier, Performance of La0.5Sr1.5MnO4±δ Ruddlesden-Popper manganite as electrode material for symmetrical solid oxide fuel cells. Part A. The oxygen reduction reaction, Electrochim. Acta. 304 (2019) 415–427. https://doi.org/10.1016/j.electacta.2019.03.037.

[20] F. Mauvy, C. Lalanne, J. Bassat, J. Grenier, H. Zhao, P. Dordor, P. Stevens, Oxygen reduction on porous LnNiO electrodes, J. Eur. Ceram. Soc. 25 (2005) 2669–2672. https://doi.org/10.1016/j.jeurceramsoc.2005.03.120.

[21] B.C. Chakoumakos, Systematics of the pyrochlore structure type, ideal A2B2X6Y, J. Solid State Chem. 53 (1984) 120–129. https://doi.org/10.1016/0022-4596(84)90234-2.

[22] L. Kong, I. Karatchevtseva, D.J. Gregg, M.G. Blackford, R. Holmes, G. Triani, Gd2Zr2O7 and Nd2Zr2O7 pyrochlore prepared by aqueous chemical synthesis, J. Eur. Ceram. Soc. 33 (2013) 3273–3285. https://doi.org/10.1016/j.jeurceramsoc.2013.05.011.

[23] B. Paul, K. Singh, T. Jaroń, A. Roy, A. Chowdhury, Structural properties and the fluorite–pyrochlore phase transition in La 2 Zr 2 O 7 : The role of oxygen to induce local disordered states, J. Alloys Compd. 686 (2016) 130–136. https://doi.org/10.1016/j.jallcom.2016.05.347.

[24] A. Montenegro-Hernández, J. Vega-Castillo, L. Mogni, A. Caneiro, Thermal stability of Ln2NiO4+δ (Ln: La, Pr, Nd) and their chemical compatibility with YSZ and CGO solid electrolytes, Int. J. Hydrogen Energy. 36 (2011) 15704–15714. https://doi.org/10.1016/j.ijhydene.2011.08.105.

[25] A. Montenegro-Hernández, A. Soldati, L. Mogni, H. Troiani, A. Schreiber, F. Soldera, A. Caneiro, Reactivity at the Ln2NiO4+δ/electrolyte interface (Ln = La, Nd) studied by Electrochemical Impedance Spectroscopy and Transmission Electron Microscopy, J. Power Sources. 265 (2014) 6–13. https://doi.org/10.1016/j.jpowsour.2014.04.082.

[26] J.M.D. Coey, M. Viret, S. von Molnár, Mixed-valence manganites, Adv. Phys. 48

(1999) 167–293. https://doi.org/10.1080/000187399243455.

[27] Y.D. Tretyakov, E.A. Goodilin, D. V Peryshkov, D.M. Itkis, Structural and microstructural features of functional materials based on cuprates and manganites, Russ. Chem. Rev. 73 (2004) 881–898. https://doi.org/10.1070/RC2004v073n09ABEH000920.

[28] V.F. Balakirev, Y. V. Golikov, Phase relations in alkaline earth-manganese-oxygen systems: Equilibrium and metastable states, Inorg. Mater. 42 (2006) S49–S69. https://doi.org/10.1134/S0020168506130036.

[29] Z.L. Moreno Botello, A. Montenegro, N. Grimaldos Osorio, M. Huvé, C. Pirovano, D.R. Småbråten, S.M. Selbach, A. Caneiro, P. Roussel, G.H. Gauthier, Pure and Zr-doped YMnO 3+δ as a YSZ-compatible SOFC cathode: a combined computational and experimental approach, J. Mater. Chem. A. 7 (2019) 18589–18602. https://doi.org/10.1039/C9TA04912F.

[30] Z.L. Moreno Botello, A. Caneiro, P. Roussel, G. Gauthier, Synthesis and preliminary study of pure and Zr-doped YMnO3 compounds as Solid Oxide Fuel Cells electrode, J. Alloys Compd. 690 (2017) 348–355. https://doi.org/10.1016/j.jallcom.2016.08.125.

[31] S.T. Norberg, S. Hull, S.G. Eriksson, I. Ahmed, F. Kinyanjui, J.J. Biendicho, Pyrochlore to Fluorite Transition: The Y 2 (Ti 1– x Zr x) 2 O 7 (0.0 ≤ x ≤ 1.0) System, Chem. Mater. 24 (2012) 4294–4300. https://doi.org/10.1021/cm301649d.

[32] S. Remsen, B. Dabrowski, Synthesis and Oxygen Storage Capacities of Hexagonal Dy 1– x Y x MnO 3+δ, Chem. Mater. 23 (2011) 3818–3827. https://doi.org/10.1021/cm2006956.

[33] C. Abughayada, B. Dabrowski, S. Kolesnik, D.E. Brown, O. Chmaissem,

Characterization of Oxygen Storage and Structural Properties of Oxygen-Loaded Hexagonal R MnO 3+δ (R = Ho, Er, and Y), Chem. Mater. 27 (2015) 6259–6267. https://doi.org/10.1021/acs.chemmater.5b01817.

[34] A. Klimkowicz, K. Cichy, O. Chmaissem, B. Dabrowski, B. Poudel, K. Świerczek, K.M. Taddei, A. Takasaki, Reversible oxygen intercalation in hexagonal Y 0.7 Tb 0.3 MnO 3+δ : toward oxygen production by temperature-swing absorption in air, J. Mater. Chem. A. 7 (2019) 2608–2618. https://doi.org/10.1039/C8TA09235D.

[35] B.B. Van Aken, A. Meetsma, T.T.M. Palstra, Hexagonal LuMnO 3 revisited, Acta Crystallogr. Sect. E Struct. Reports Online. 57 (2001) i101–i103. https://doi.org/10.1107/S1600536801015896.

[36] A.S. Gibbs, K.S. Knight, P. Lightfoot, High-temperature phase transitions of hexagonal YMnO3, Phys. Rev. B. 83 (2011) 094111. https://doi.org/10.1103/PhysRevB.83.094111.

[37] Q.H. Zhang, X. Shen, Y. Yao, Y.G. Wang, C.Q. Jin, R.C. Yu, Oxygen vacancy ordering and its mobility in YMnO3, J. Alloys Compd. 648 (2015) 253–257. https://doi.org/10.1016/j.jallcom.2015.07.032.

[38] A. Veres, J.G. Noudem, S. Fourrez, G. Bailleul, The influence of iron substitution to manganese on the physical properties of YMnO3, Solid State Sci. 8 (2006) 137–141. https://doi.org/10.1016/j.solidstatesciences.2005.11.002.

[39] A. Caneiro, P. Bavdaz, J. Fouletier, J.P.P. Abriata, Adaptation of an electrochemical system for measurement and regulation of oxygen partial pressure to a symmetrical thermogravimetric analysis system developed using a Cahn 1000 electrobalance, Rev. Sci. Instrum. 53 (1982) 1072–1075. https://doi.org/10.1063/1.1137090.

[40] J.-L. Dellis, No Title, (2014). http://www.mathworks.com/matlabcentral/fileexchange/19460-zfit.

[41] L. Baqué, Preparación y caracterización de cátodos de alto rendimiento para celdas de combustible de óxido sólido de temperatura intermedia, Instituto Balseiro, 2011.

[42] V. V Srdi, R.P. Omorjan, J. Seydel, Electrochemical performances of (La , Sr) CoO 3 cathode for zirconia-based solid oxide fuel cells, Mater. Sci. Eng. B. 116 (2005) 119–124. https://doi.org/10.1016/j.mseb.2004.07.075.

[43] L. V. Mogni, Estudio de nuevos conductores mixtos para aplicaciones electroquímicas de alta temperatura, Instituto Balseiro, 2007.

[44] D.A. Garcés, Estudio de perovskitas LaBaCo2O6-δ: Propiedades de alta temperatura y su evaluación como potenciales materiales para celdas de combustible o electrolíticas de óxido sólido, Instituto Balseiro, 2014.

[45] L. V Mogni, Estudio de nuevos conductores mixtos para aplicaciones electroquímicas de alta temperatura, Asoc. Argentina Mater. 5 (2008) 14–23.

[46] J. Nielsen, J. Hjelm, Impedance of SOFC electrodes: A review and a comprehensive case study on the impedance of LSM:YSZ cathodes, Electrochim. Acta. 115 (2014) 31–45. https://doi.org/10.1016/j.electacta.2013.10.053.

[47] A. Kromp, Model-based Interpretation of the Performance and Degradation of Reformate, KIT Scientific Publishing, 2013.

[48] S.B. Adler, J.A. Lane, B.C.H. Steele, Electrode Kinetics of Porous Mixed − Conducting Oxygen Electrodes, J. Electrochem. Soc. 143 (1996) 3554–3564. https://doi.org/10.1149/1.1837252.

[49] S. Adler, X. Chen, J. Wilson, Mechanisms and rate laws for oxygen exchange on

mixed-conducting oxide surfaces, J. Catal. 245 (2007) 91–109. https://doi.org/10.1016/j.jcat.2006.09.019.

[50] A. Montenegro-Hernández, Estudio de reacción de electrodo de compuestos Ln2NiO4+d (Ln: La, Pr Y Nd) Y reactividad con diferentes electrolitos, Doctorado, Instituto Balseiro - U.N. de Cuyo, 2013.

[51] B.H. Park, G.M. Choi, Electrochemical performance and stability of La0.2Sr0.8Ti0.9Ni0.1O3-δ and La0.2Sr0.8Ti0.9Ni0.1O3-δ - Gd0.2Ce0.8O2-δ anode with anode interlayer in H2 and CH4, Electrochim. Acta. 182 (2015) 39–46. https://doi.org/10.1016/j.electacta.2015.09.017.

Figure Captions

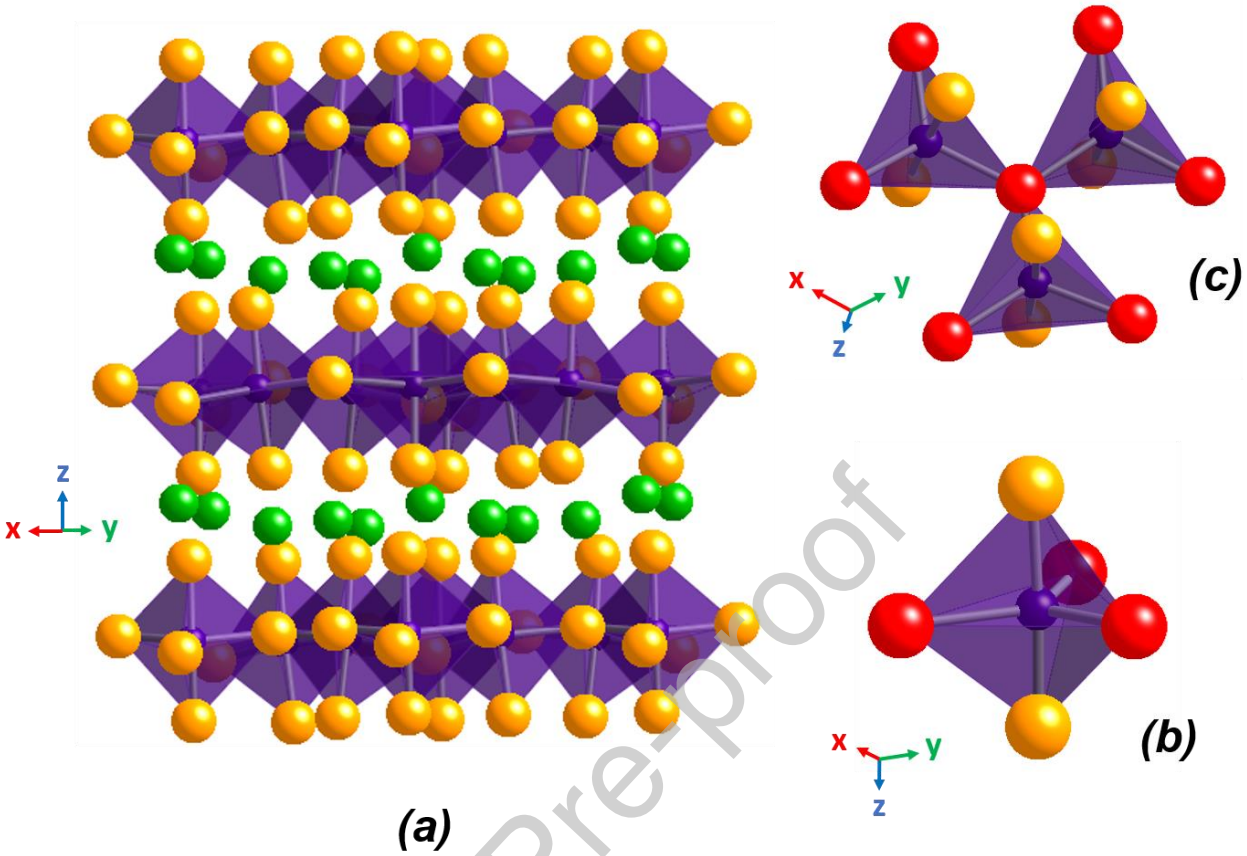

Figure 1. (a) $YMnO_3$ crystal structure showing the laminar arrangement made of (b) MnO_5 trigonal bi-pyramids that are (c) joined by corners. Mn in violet, Y in green and O in yellow. In (b,c), equatorial oxygen atoms are evidenced in red while apical oxygen atoms are left in yellow.

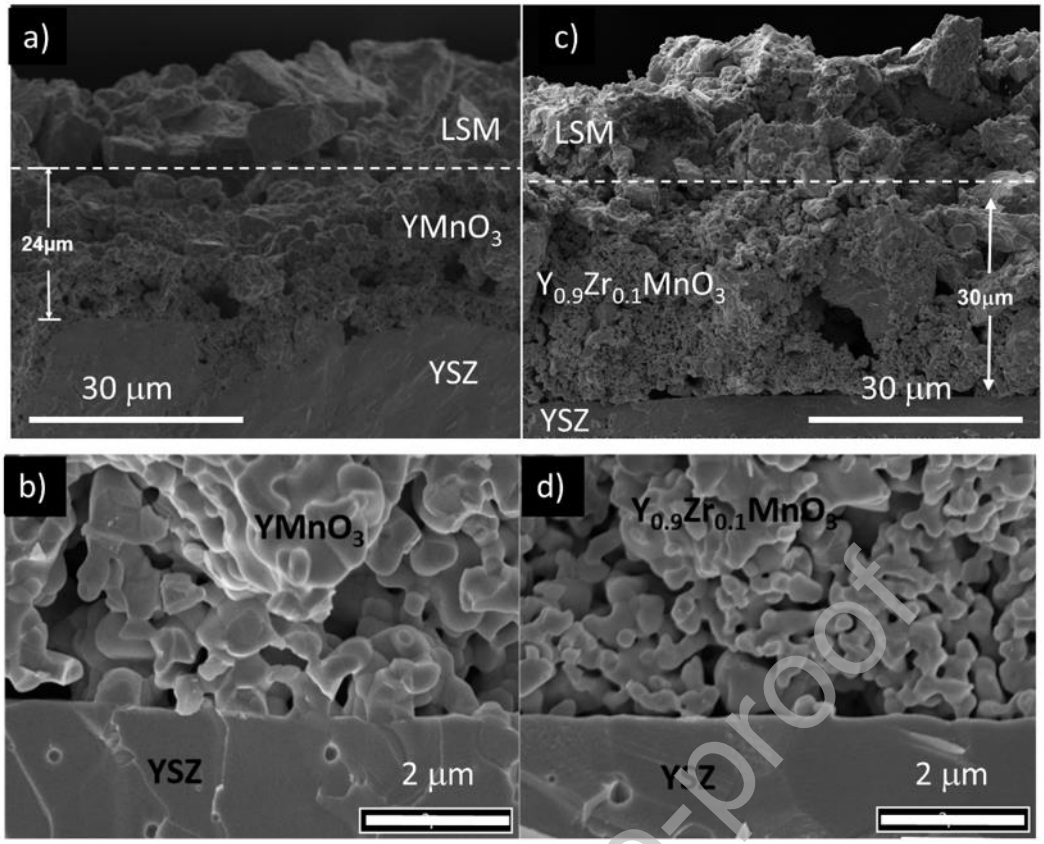

Figure 2. SEM images of the electrode microstructure for (a) LSM/$YMnO_3$/YSZ/$YMnO_3$/LSM and (b) LSM/$Y_{0.9}Zr_{0.1}MnO_3$/YSZ/$Y_{0.9}Zr_{0.1}MnO_3$/LSM symmetric cells. (c) and (d) shows a detail of $YMnO_3$/YSZ and $Y_{0.9}Zr_{0.1}MnO_3$/YSZ interfaces, respectively, after thermal treatment at 1150 °C.

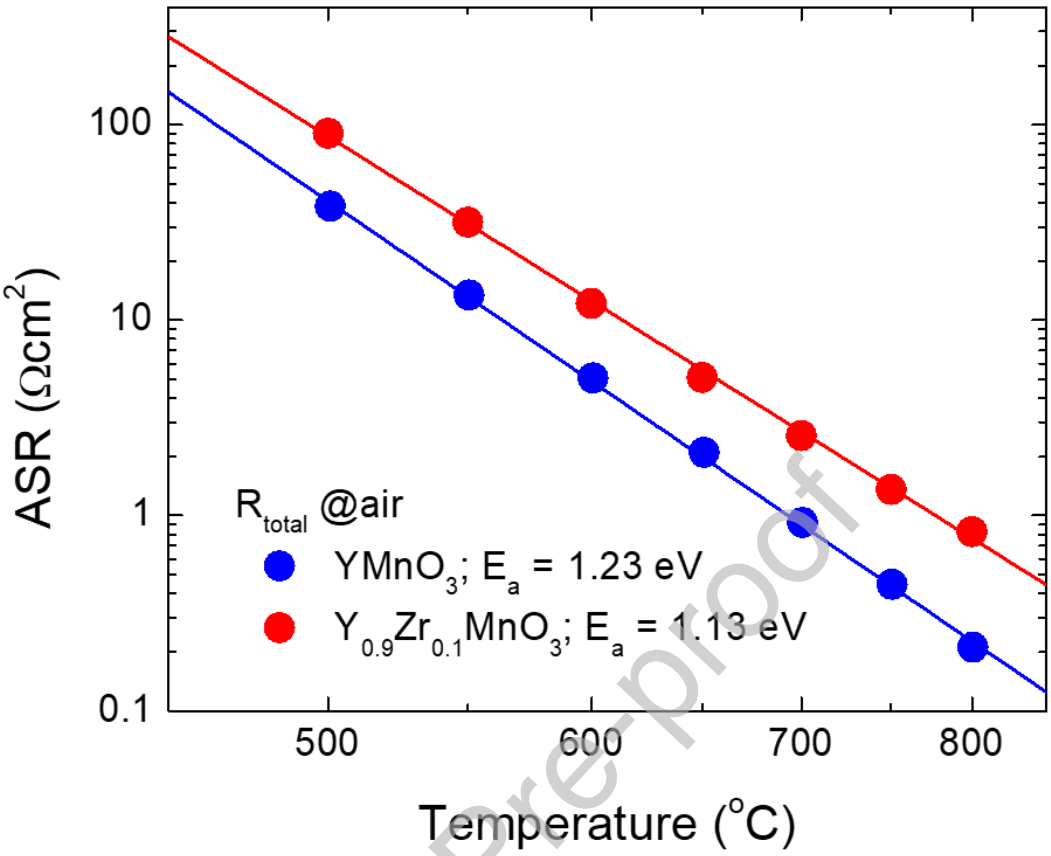

Figure 3. Dependence of the area specific resistance (ASR) with temperature for the symmetrical cells with $YMnO_3$ and $Y_{0.9}Zr_{0.1}MnO_3$ electrodes heat-treated at 1150 ºC.

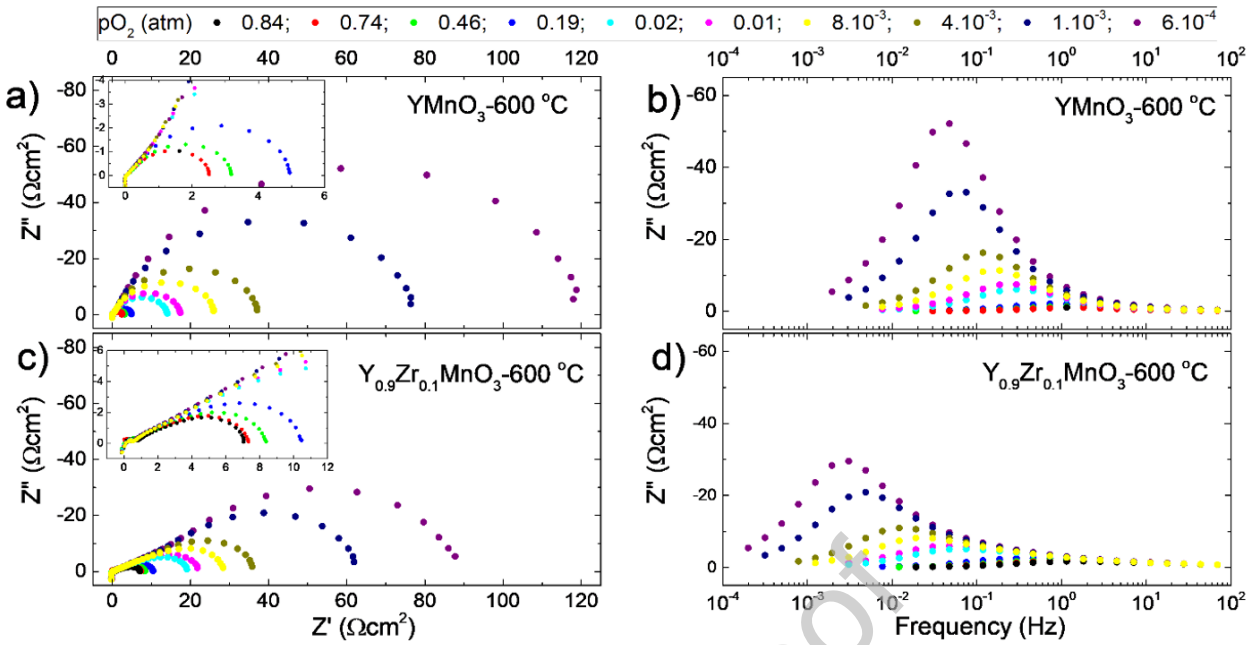

Figure 4. (a)-(b) Nyquist and (c)-(d) Bode representation of impedance spectra for LSM/$YMnO_3$/YSZ/$YMnO_3$/LSM and LSM/$Y_{0.9}Zr_{0.1}MnO_3$/YSZ/$Y_{0.9}Zr_{0.1}MnO_3$/LSM cells measured at T=600°C for different pO_2 values. A zoom in the high pO_2 range was inserted in the corresponding figures.

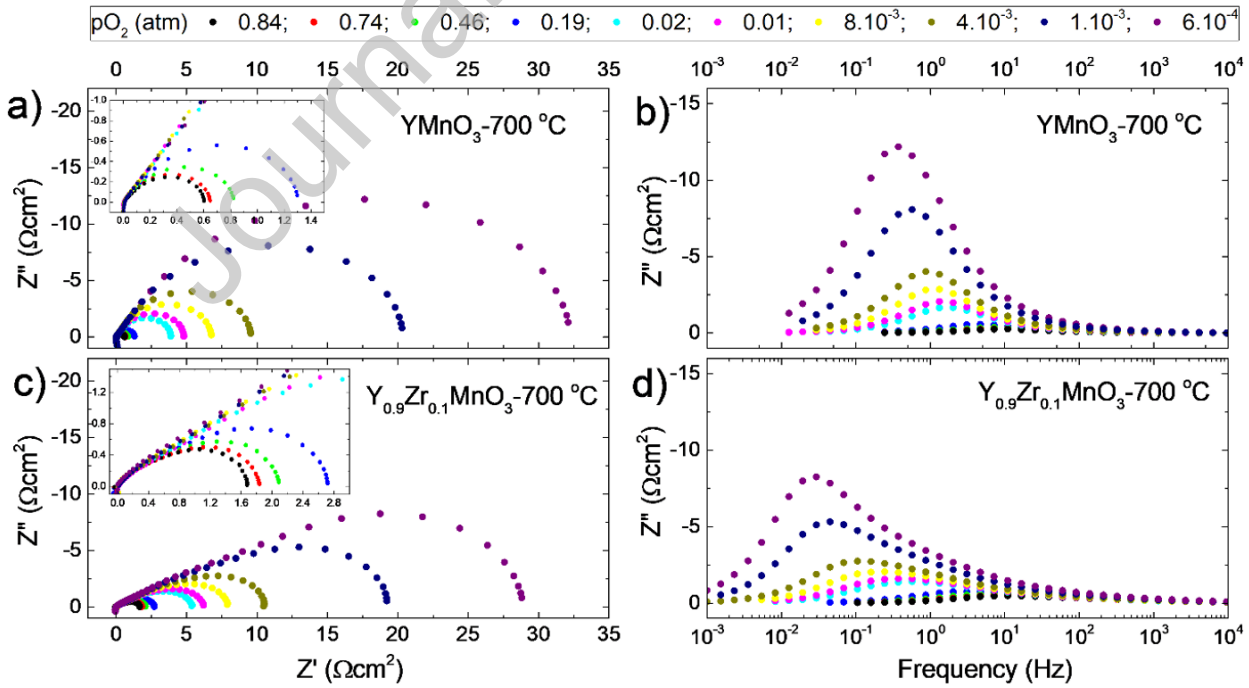

Figure 5. (a)-(b) Nyquist and (c)-(d) Bode representation of impedance spectra for LSM/$YMnO_3$/YSZ/$YMnO_3$/LSM and LSM/$Y_{0.9}Zr_{0.1}MnO_3$/YSZ/$Y_{0.9}Zr_{0.1}MnO_3$/LSM cells measured at T=700°C for different pO_2 values. A zoom in the high pO_2 range was inserted in the corresponding figures.

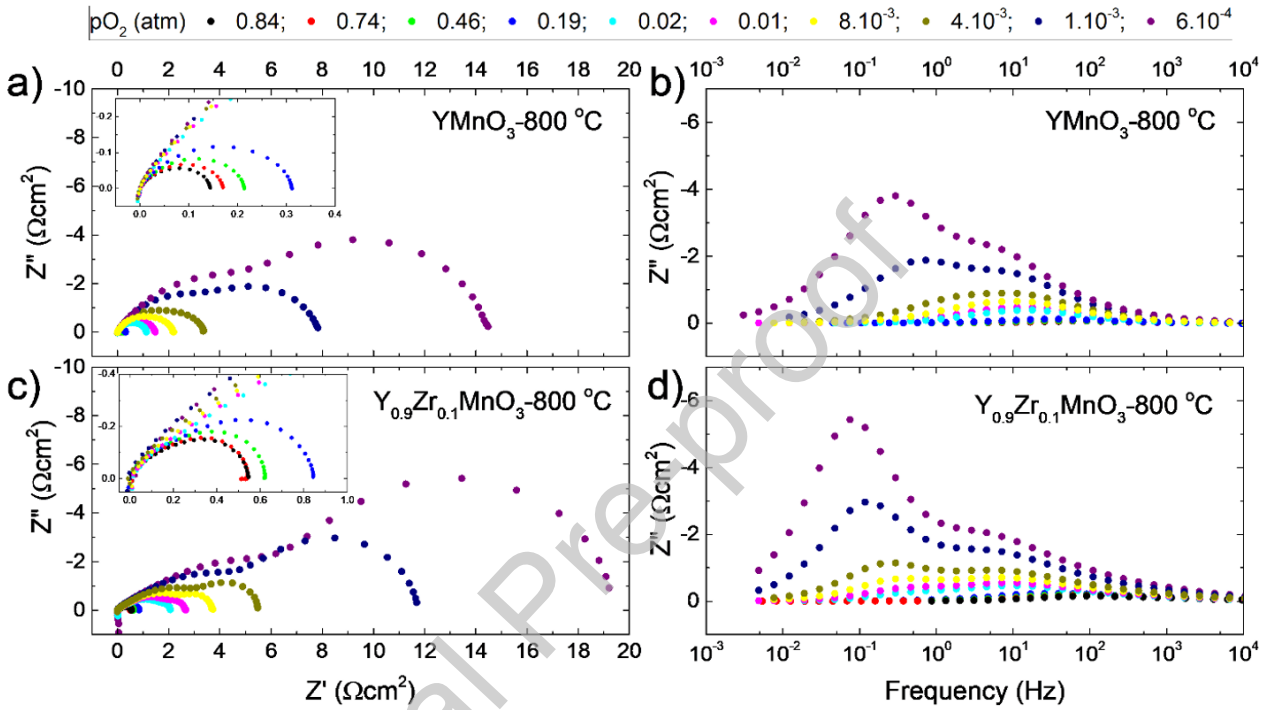

Figure 6. (a)-(b) Nyquist and (c)-(d) Bode representation of impedance spectra for LSM/$YMnO_3$/YSZ/$YMnO_3$/LSM and LSM/$Y_{0.9}Zr_{0.1}MnO_3$/YSZ/$Y_{0.9}Zr_{0.1}MnO_3$/LSM cells measured at T=800°C for different pO_2 values. A zoom in the high pO_2 range was inserted in the corresponding figures.

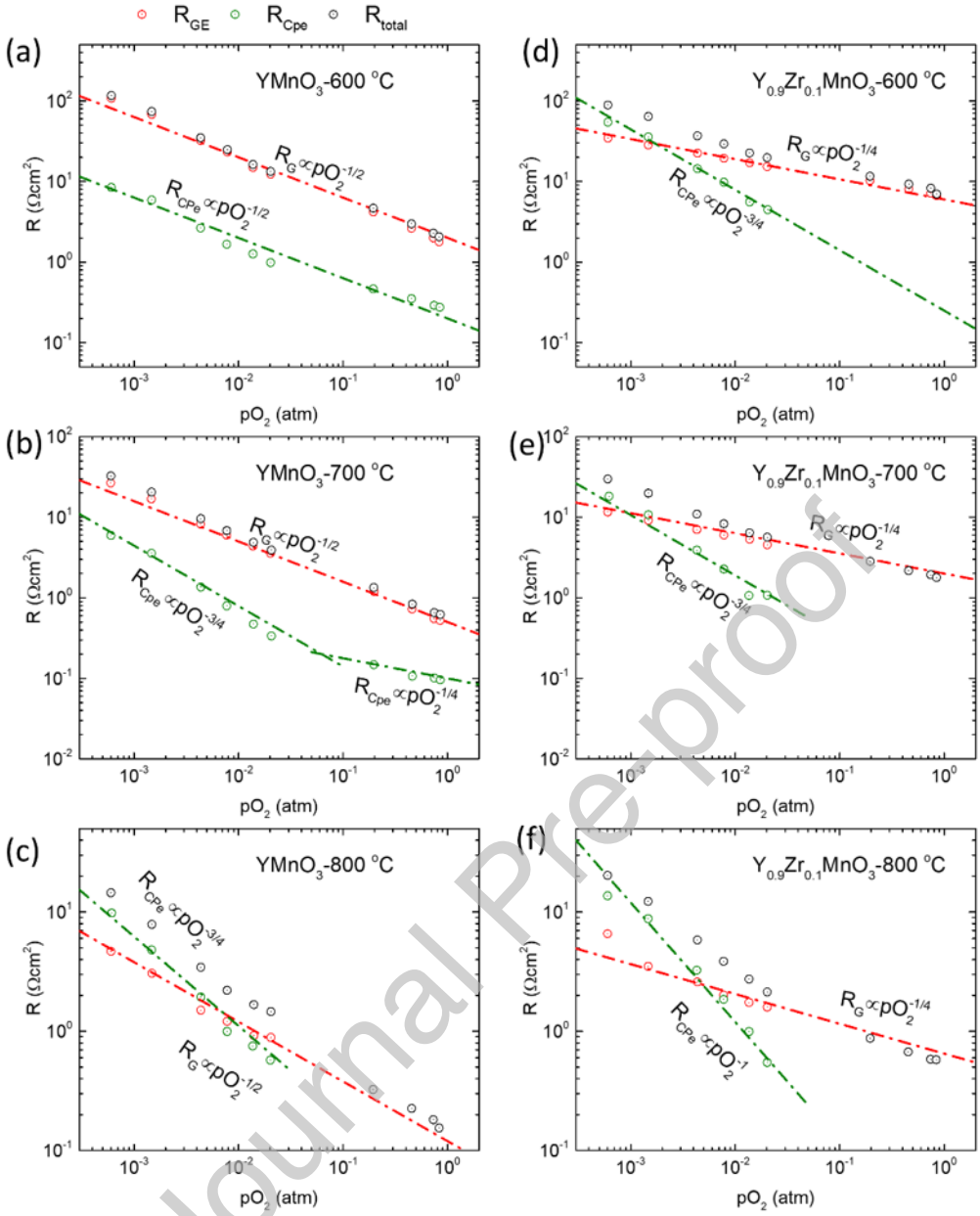

Figure 7. Evolution of the polarization resistance for the intermediate frequency Gericher-like impedance (R_G) and the low frequency element R//CPE (R_{Cpe}) as a function of pO_2 for LSM/$YMnO_3$/YSZ/$YMnO_3$/LSM cell measured at (a) 600, (b) 700 and (c) 800°C and for LSM/$Y_{0.9}Zr_{0.1}MnO_3$/YSZ/$Y_{0.9}Zr_{0.1}MnO_3$/LSM cell measured at (d) 600, (e) 700 and (f) 800°C. The reaction order with respect to pO_2 is also included for each step.

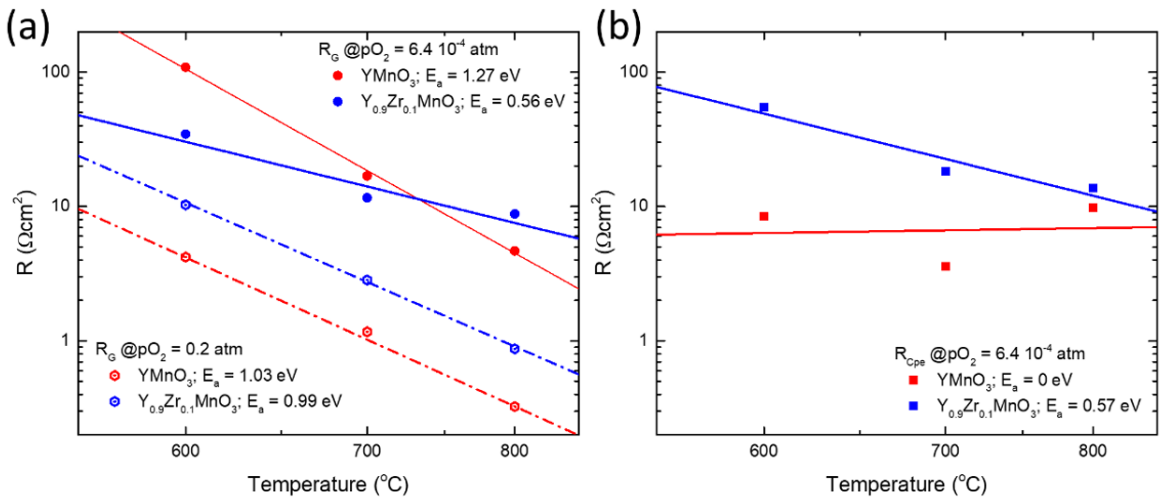

Figure 8. Plots of a) RG and b) RCpe at low (6.4 10^{-4} atm) and high (0.2 atm) pO_2 as a function of temperature. The activation energy (Ea) of impedance elements is obtained from Arrhenius plot and indicated in the graph for $YMnO_3$ (red) and $Y_{0.9}Zr_{0.1}MnO_3$ (blue) electrodes.

Table 1. Summary of main characteristics of the components of the EEC used to fit the electrochemical impedance response. EEC includes a inductive element (L_1-wire), an ohmic resistance (R_{el}-electrolyte), a high frequency (HF) parallel combination of one resistance and one constant phase element (R//CPE- only present at 600 °C), a Gerischer-type element (G), and a R//CPE element at low frequencies. The R//CPE is observed at low pO_2.

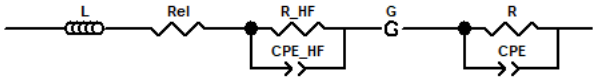

	T (°C)	Gerischer-type Z_G			Low frequency $Z_{R//Cpe}$		
		~n (*$R \propto (pO_2)^n$*)	~C (F/cm^2)	Ea (eV) low-high pO_2	*~n* (*$R \propto (pO_2)^n$*)	~C (F/cm^2)	Ea (eV) low pO_2
$YMnO_3$	600	-½ (-0.45)	10^{-2}-10^{-1}	1.27-1.03	- ½ (-0.55)	0.05	0
	700	-½(-0.56)	10^{-2}		- ½ (-0.54)	10^{-2}	
	800	-½ (-0.44)	10^{-2}		-¾ and -1 (-0.83)	10^{-2}	
$Y_{0.9}Zr_{0.1}MnO_3$	600	-¼ (-0.22)	10^{-2}-10^{-1}	0.56-0.99	-¾ (-0.75)	1	0.57
	700	-¼ (-0.25)	10^{-2}		-¾ and -1 (-0.85)	10^{-1}-1	
	800	-¼ (-0.30)	10^{-3}-10^{-2}		-¾ and -1 (-0.91)	10^{-1}	